



## Probing the bandgap and effects of t-BN domains in h-BN neutron detectors

Attasit Tingsuwatit, Jing Li, Jingyu Lin\*, and Hongxing Jiang\*

Department of Electrical and Computer Engineering, Texas Tech University, Lubbock, TX 79409, United States of America

\*E-mail: [jingyu.lin@ttu.edu](mailto:jingyu.lin@ttu.edu); [hx.jiang@ttu.edu](mailto:hx.jiang@ttu.edu)

Received August 28, 2022; revised September 8, 2022; accepted September 11, 2022; published online September 22, 2022

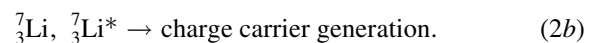
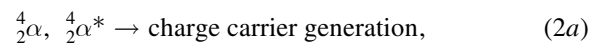
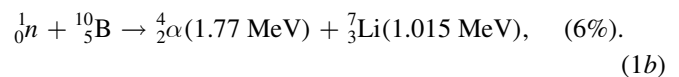
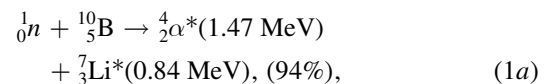
Thermal neutron detectors in a lateral scheme were fabricated from a 70  $\mu\text{m}$  thick freestanding B-10 enriched hexagonal BN (h- $^{10}\text{B}$ N). Two sets of channel peaks corresponding to the neutron capture by  $^{10}\text{B}$  occurring in h- $^{10}\text{B}$ N comprising turbostratic domains (t- $^{10}\text{B}$ N) have been recognized in the nuclear reaction pulsed height spectrum, from which a bandgap of 5.5 eV was directly deduced for t- $^{10}\text{B}$ N. Improved device performance over the prior state-of-the-art implies that the transport properties in the lateral plane of t-BN domains are sufficiently good and their presence in h-BN is not a showstopper for the further advancement of h-BN detector technologies. © 2022 The Japan Society of Applied Physics

Progress made in the last 30 years in III-nitride wide bandgap semiconductors has already revolutionized the lighting and power electronics industries.<sup>1,2)</sup> Among III-nitrides, hexagonal BN (h-BN) with an ultrawide bandgap ( $\sim 6.1$  eV) is considered a remaining frontier with many unique properties.<sup>3–18)</sup> These include a large optical absorption coefficient ( $7.5 \times 10^5 \text{ cm}^{-1}$ ) resulting in an extremely small optical absorption length of about 15 nm for the above bandgap photons,<sup>3,4)</sup> huge excitonic effects,<sup>7,8)</sup> a more feasible p-type conductivity control than AlN<sup>9–12)</sup> and point defects exhibiting single photon emitters which are optically stable<sup>13–16)</sup> and capable to operate at elevated temperatures.<sup>17)</sup> Another unique aspect of h-BN is that it is also an ideal material for the realization of solid-state direct-conversion thermal neutron detectors with high efficiency and sensitivity.<sup>11,12,18–20)</sup> This is because  $^{10}\text{B}$  isotope is among a few elements having a significant capture cross section ( $\sigma$ ) for thermal neutrons ( $\sigma = 3840$  barns or  $3.84 \times 10^{-21} \text{ cm}^2$  for  $^{10}\text{B}$ ).<sup>21)</sup>

Compared to He-3 gas detectors, semiconductor detectors offer obvious advantages of reduced size and weight, lower operating voltage and power consumption, elimination of pressurization, and lower costs of operation/maintenance. In contrast to existing indirect-conversion semiconductor detectors which rely on coating a thin neutron conversion layer of  $^6\text{Li}$  or  $^{10}\text{B}$  on a bulk semiconductor<sup>22–25)</sup> or formation of micro-structures filled with a  $^{10}\text{B}$  or  $^6\text{Li}$  neutron conversion material<sup>26–28)</sup> with a limited theoretical detection efficiency, the same h- $^{10}\text{B}$ N layer performs the functions of neutron absorption and charge collection, and therefore the theoretical detection efficiency of h- $^{10}\text{B}$ N thermal neutron detectors can approach 100%. As an ultrawide bandgap semiconductor, h- $^{10}\text{B}$ N detectors are capable to operate in extreme conditions.<sup>29)</sup> Recently, we have reported the successful growth by metal-organic chemical vapor deposition (MOCVD) of freestanding B-10 enriched h-BN (h- $^{10}\text{B}$ N) wafers (4 inches in diameter) with a thickness up to 200  $\mu\text{m}$ <sup>19)</sup> and realization of a large area (1  $\text{cm}^2$ ) thermal neutron detectors from 100  $\mu\text{m}$  thick h- $^{10}\text{B}$ N by combining 5 lateral detector strips with a record high detection efficiency of 59%.<sup>20)</sup> These results demonstrated the promise of BN semiconductor neutron detectors to replace He-3 gas-based technology for various applications.

The principle of h- $^{10}\text{B}$ N semiconductor thermal neutron detectors is based on the nuclear reaction described by the

following equations<sup>21)</sup>:



The nuclear reaction of Eq. (1) produces  $\alpha$  and Li particles, which generate charge carriers described by Eq. (2). The collection of these charge carriers under a bias voltage indicates the detection of thermal neutrons. The density of  $^{10}\text{B}$  atoms in B-10 enriched h-BN (h- $^{10}\text{B}$ N) is  $N(^{10}\text{B}) = 5.5 \times 10^{22} \text{ cm}^{-3}$ , which provides an absorption coefficient of  $\alpha = N\sigma = 5.5 \times 10^{22} \times 3.84 \times 10^{-21} = 211.2 \text{ cm}^{-1}$ , absorption length of  $\lambda = \alpha^{-1} = 47.3 \mu\text{m}$  and intrinsic detection efficiency for thermal neutrons of

$$\eta_i(t) = 1 - e^{-t/\lambda} \quad (3)$$

in h- $^{10}\text{B}$ N, where  $t$  is the detector's layer thickness. Based on Eq. (3), h- $^{10}\text{B}$ N thermal neutron detectors require a thickness of 47.3  $\mu\text{m}$  (1  $\lambda$ ) to have a theoretical detection efficiency of 63%, which is in sharp contrast to the thickness requirement of h-BN photonic devices with an optical absorption length of 15 nm for the above bandgap photons.<sup>3,4)</sup> This large thickness requirement poses a great challenge for epitaxial growth, especially given the fact that the growth of h-BN is still in an early stage of development compared to other III-nitride materials. The best measured detection efficiency for a 100  $\mu\text{m}$  thick h- $^{10}\text{B}$ N detector so far is 59% at a bias voltage of 500 V.<sup>20)</sup> However, the expected intrinsic efficiency ( $\eta_i$ ) is 88% for a 100  $\mu\text{m}$  thick h- $^{10}\text{B}$ N thermal neutron detector based on Eq. (3). While  $\eta_i$  scales with the detector's thickness following Eq. (3), the total detection efficiency is also affected by the charge collection efficiency which is controlled predominantly by the overall material quality of h- $^{10}\text{B}$ N. Previous studies revealed strong evidence that oxygen and its related defects are detrimental to the charge collection efficiency of h- $^{10}\text{B}$ N neutron detectors.<sup>11,12,18–20,30)</sup>

Moreover, during MOCVD growth of h-BN using relatively high growth rates, various polytype domains may be incorporated and the stacking sequence may also be random to form turbostratic BN (t-BN) domains inside h-BN because

the stacking sequence has only a minor effect on the total energy of the layer-structured BN crystals.<sup>31)</sup> The presence of *t*-BN domains in *h*-BN layers has been confirmed previously by X-ray diffraction (XRD) and ellipsometry measurements.<sup>32–35)</sup> In our thick *h*-<sup>10</sup>BN films grown by MOCVD, XRD  $\theta$ - $2\theta$  scan revealed the presence of two separate diffraction peaks with a main peak at  $26.59^\circ$  due to *h*-<sup>10</sup>BN and a side peak at  $\sim 26.1^\circ$  associated with *t*-<sup>10</sup>BN domains within *h*-<sup>10</sup>BN.<sup>35)</sup> Since it is challenging to eliminate *t*-BN domains in thick *h*-BN films in the near term, understanding their influence on the detection efficiency becomes relevant and necessary for further advancing the BN neutron detector technology. We report here the fabrication and utilization of a lateral *h*-BN thermal neutron detector for directly probing the effects of *t*-BN domains on the *h*-BN thermal neutron detector performance. Remarkably, the energy bandgap of *t*-BN can also be derived directly from the nuclear reaction pulsed height spectrum.

B-10 enriched *h*-BN wafers were grown on *c*-plane sapphire of 4 inches in diameter using MOCVD. As described in our previous works,<sup>11,12,18–20)</sup> B-10 enriched trimethylboron (TMB) and ammonia (NH<sub>3</sub>) were used as the precursors for B-10 and N, respectively. To reduce the

oxygen diffusion from the sapphire substrate into *h*-<sup>10</sup>BN layers, multiple thin BN buffer layers with a total thickness of about 100 nm were first grown at  $\sim 800^\circ\text{C}$  to  $1000^\circ\text{C}$ , which was then followed by the growth of the *h*-<sup>10</sup>BN active layer at a temperature of  $\sim 1400^\circ\text{C}$ . A freestanding *h*-<sup>10</sup>BN wafer was obtained by self-separation from the sapphire substrate after cooling down, as illustrated in inset (a) of Fig. 1(a). The inset (b) of Fig. 1(a) is a photo of a freestanding *h*-<sup>10</sup>BN wafer of  $\sim 70\ \mu\text{m}$  in thickness. As illustrated in the inset (a) of Fig. 1(b), detector strips in a lateral scheme with 1 mm in width and 1 cm in length were then fabricated via laser dicing and metallization to take the advantage of *h*-BN's lateral transport properties.<sup>12)</sup> Electrodes were formed by depositing a bi-layer of Ni (100 nm)/Au (40 nm) on the two edges of the *h*-<sup>10</sup>BN strip using e-beam evaporation leaving around  $\sim 100\ \mu\text{m}$  metal covering on the edges. The electrodes were bonded to the bonding pads of a semiconductor device package for characterization. A typical dark current–voltage characteristic of these  $1\ \text{cm} \times 1\ \text{mm}$  detector strips is shown in Fig. 1(a), yielding an electrical resistivity of  $3.5 \times 10^{13}\ \Omega\text{-cm}$ , which is about one order of magnitude larger than our previous attainment of  $1 \times 10^{12}\ \Omega\text{-cm}$ <sup>20)</sup> and is most likely due to the insertion of multiple *h*-BN buffer layers prior to the growth of the final active *h*-<sup>10</sup>BN layer. A micrograph of a fabricated detector strip mounted on sapphire via a layer of highly resistive adhesive polyimide is shown as inset (b) in Fig. 1(b).

To assess the thermal neutron detection efficiency, a Californium-252 (<sup>252</sup>Cf) source from Frontier Technology was used as a neutron source. The calibrated fast neutron emission rate at the time of measurement was  $7.3 \times 10^5$  neutrons per second (n/s). A high-density polyethylene (HDPE) cube moderator of 2.5 cm in thickness was used to house the neutron source and to convert fast neutrons to thermal neutrons.<sup>11,12,18–20,36)</sup> The *h*-<sup>10</sup>BN detector and a commercial <sup>6</sup>LiF filled  $4\ \text{cm}^2$  micro-structured semiconductor neutron detector (MSND Domino™ V4) with a certified detection efficiency of 30% were placed side-by-side at 30 cm from the HDPE surface and exposed to thermal neutrons for 20 min, the detection efficiencies ( $\eta$ ) of the *h*-<sup>10</sup>BN detector at various bias voltages were obtained by calibrating against that of MSND.

Traditionally, the charge collection efficiency of a detector is defined as the ratio of the number of charge carriers collected to the total number of charge carriers generated. In the case of *h*-<sup>10</sup>BN neutron detectors, the neutron will be detected and counted as long as the neutron-generated signal (via charge carrier generation by  $\alpha$  and Li particles and collection by electrodes) can trigger a voltage pulse above the low-level discriminator set in the electronics. As such, we use the ratio of  $\eta/\eta_i$  for the purpose of making a comparison of the abilities of charge collection among different devices as well as for a device operating under different conditions. Here,  $\eta$  is the measure of detection efficiency and  $\eta_i$  is the theoretical efficiency defined by Eq. (3), and so  $\eta/\eta_i$  describes the deviation from  $\eta_i$ .

From the measured values of  $\eta$  and known thickness of  $70\ \mu\text{m}$ , the values of  $\eta/\eta_i$  can be obtained and the results are shown in Fig. 1(b), demonstrating a value of  $\eta/\eta_i \approx 90\%$  at a bias voltage of 550 V, while the previous  $100\ \mu\text{m}$  thick *h*-<sup>10</sup>BN thermal neutron detector with a detection efficiency

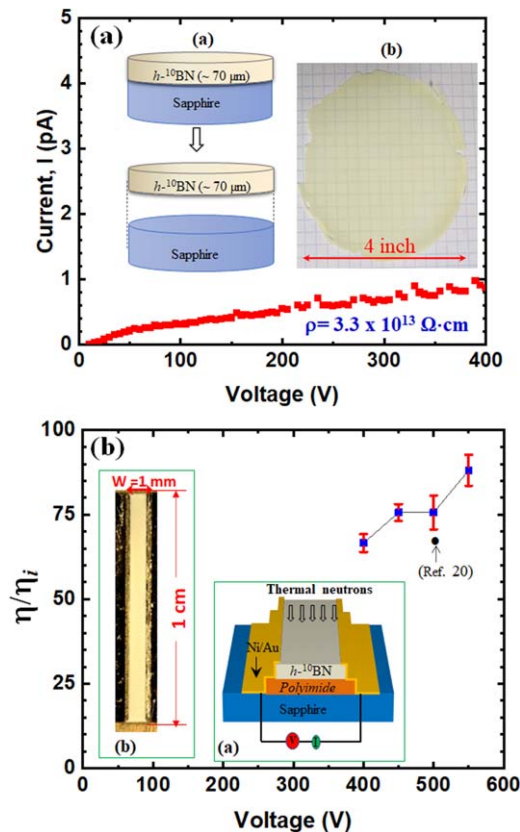


**Fig. 1.** (Color online) (a) Dark current–voltage characteristic of a *h*-<sup>10</sup>BN detector strip (1 cm in length and 1 mm in width) fabricated from a  $70\ \mu\text{m}$  thick freestanding *h*-<sup>10</sup>BN wafer. Inset (a) shows a schematic illustration of a freestanding *h*-<sup>10</sup>BN wafer formation by self-separation. Inset (b) is a photo of a freestanding *h*-<sup>10</sup>BN wafer 4 inches in diameter. (b) The ratio of  $\eta/\eta_i$  of a *h*-<sup>10</sup>BN detector (1 cm in length and 1 mm in width) fabricated from a  $70\ \mu\text{m}$  thick freestanding *h*-<sup>10</sup>BN wafer as a function of the applied bias voltage, where the detection efficiency ( $\eta$ ) values were obtained by calibrating against a commercial MSND detector and  $\eta_i$  is the theoretical detection efficiency described by Eq. (3). The black dot represents the measured value of  $\eta/\eta_i$  of a previous  $100\ \mu\text{m}$  thick *h*-<sup>10</sup>BN thermal neutron detector with a record high detection efficiency of  $\eta = 59\%$  at 500 V [20]. Inset (a) and inset (b) are, respectively, the schematic and photo of a finished lateral *h*-<sup>10</sup>BN detector strip.

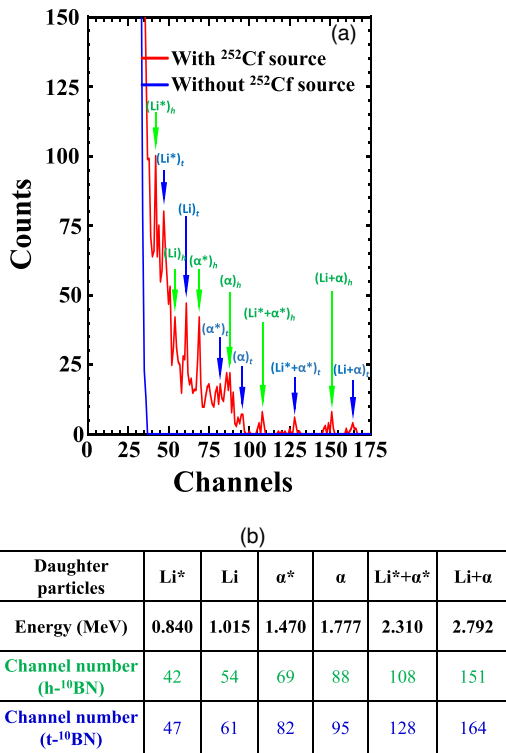


**Fig. 2.** (Color online) A representative pulsed height spectra of a h-<sup>10</sup>BN detector strip (1 cm in length and 1 mm in width) fabricated from a 70 μm thick freestanding h-<sup>10</sup>BN wafer, measured at 500 V. The red spectrum was measured under thermal neutron irradiation and the blue spectrum was recorded in the absence of any radiation. The blue and green colored arrows indicate the observed peak channels corresponding to the charge generation by the nuclear reaction particles in h-<sup>10</sup>BN and t-<sup>10</sup>BN, respectively. The red spectrum (under thermal neutron irradiation) was averaged over three different measurements, each with a 20 min counting time. (b) Summary of observed nuclear reaction product peak channels in Fig. 2(a) and the expected energies of the nuclear reaction products described in Eq. (1). The higher channels (blue arrows) and lower channels (green arrows) are assigned to the reactions occurring in t-<sup>10</sup>BN and h-<sup>10</sup>BN, respectively, because  $E_g(t-^{10}\text{BN}) < E_g(h-^{10}\text{BN})$  and it takes an energy of  $3E_g$  to generate one electron-hole pair in BN.

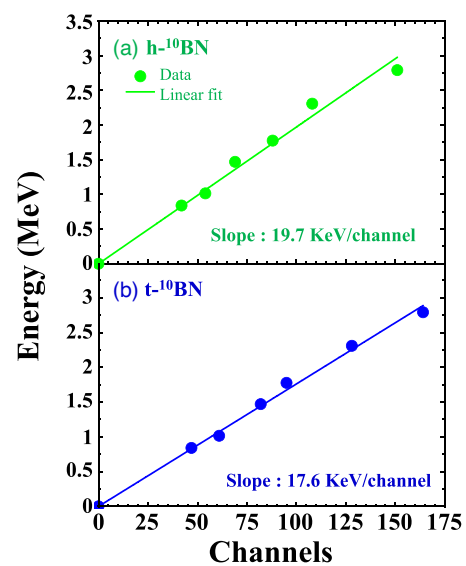
of 59% had a value of  $\eta/\eta_i = 67\%$  at 500 V.<sup>20)</sup> We believe that the improved  $\eta/\eta_i$  values over the prior state-of-the-art were made possible by fabricating strips at a small width of 1 mm as well as by using materials with reduced background impurities as reflected by the enhancement in the electrical resistivity.

Figure 2(a) shows the pulsed height spectra of the h-<sup>10</sup>BN detector measured at 500 V. The spectrum (red) was measured under thermal neutron irradiation and the dark spectrum (blue) was also recorded in the absence of any radiation. It has been proven that h-<sup>10</sup>BN detectors exhibit no response to gamma photons when directly exposed to a Cesium-137 source.<sup>18,20)</sup> This is because BN is composed of low atomic number elements. The most interesting result exhibited in Fig. 2(a) is that the pulsed height spectrum under thermal neutron irradiation resolved many sharp peaks with a high energy resolution. Such features were observed previously only in h-BN detectors fabricated from thin films (<1 μm) with high crystalline quality<sup>37)</sup> and absent in detectors fabricated from thick films.<sup>17,18,20)</sup>

In an ideal scenario, as α or Li particles move in the opposite direction upon generation (with a range of 5 μm and

2 μm, respectively), ionizing and generating electrons and holes along their track and depositing their energies in the detector, if all neutron-generated charge carriers are collected, the reaction should register primarily the sum peaks at 2.31 MeV (Li\* + α\*) and 2.79 MeV (Li + α) in the pulsed height spectrum. However, the observed spectrum shown in Fig. 2 resolves many individual peaks, similar to the features observed in a thin film h-BN detector.<sup>37)</sup> The lateral detector strip has 1 mm in width with electrodes deposited on the two edges, the α or Li particles generated near the detector’s edges or surfaces have a high probability of only depositing their energies individually. In the detector’s interior, as the electrons and holes moving toward their respective electrodes, an electric field is induced. The induced electric field distributions are most likely non-identical in cases where carriers were generated by α particle versus Li particle inside h-BN. With these considerations, the following four scenarios are possible depending on the direction of the induced line charges generated (by α or Li particles) relative to the applied field upon a neutron capture: (i) a count is triggered by either α or Li, resulting in an individual α or Li peak; (ii) a count is triggered by α and Li, resulting in the α + Li sum peak; (iii) two separate counts, one triggered by α and another by Li, resulting in individual α and Li peaks; and (iv) no count is detected because charge carriers never arrived the electrodes to be collected. These scenarios can result in individual as well as the sum peaks in the pulsed height spectrum. As h-<sup>10</sup>BN detectors represent the newest class of direct-conversion neutron detectors, detailed analysis by theory and modeling is still needed to help to understand the processes of charge generation, distribution, transport, and collection as well as the pulsed height spectral shape, which however are not the focus of the present study.

Based on Eqs. (1) and (2), we expect to resolve 6 peak channels corresponding to α, α\*, Li, Li\*, α + Li, α\* + Li\*.<sup>37)</sup> By carefully analyzing the observed peak channels according to the expected reaction products, we recognized



**Fig. 3.** (Color online) Plots of the nuclear reaction product energy ( $E$ ) of Eq. (1) versus the observed peak channel number in Fig. 2, assuming (a) the nuclear reaction occurring in h-<sup>10</sup>BN (green-colored) and (b) the nuclear reaction occurring in t-<sup>10</sup>BN. Solid dots are experimental data and solid lines are linear fits.

two sets of peaks corresponding to  $\alpha$ ,  $\alpha^*$ , Li, Li\*,  $\alpha + \text{Li}$ ,  $\alpha^* + \text{Li}$ . We believe that this is due to the presence of t-<sup>10</sup>BN domains within h-<sup>10</sup>BN. We summarize the observed peak channels and the corresponding energies of the reaction particles in a table shown as Fig. 2(b). With this understanding, we expect the following to hold: (i) energies of the nuclear reaction products, Li,  $\alpha$ , Li\*,  $\alpha^*$ ,  $\alpha + \text{Li}$ , and  $\alpha^* + \text{Li}$ \*, are the same in h-<sup>10</sup>BN and t-<sup>10</sup>BN; (ii) it takes an energy of  $3E_g$  to generate one electron–hole pair in a semiconductor with an energy gap of  $E_g$ ; (iii) for a particular daughter particle with an energy  $E$ , the number of electron–hole pairs it generates is:  $N_{e-h} = E/3E_g$ . Therefore, the observed peak channels in the pulsed height spectrum have a one-to-one relationship with the energies of the nuclear reaction products. We plot the reaction product energy ( $E$ ) versus the observed reaction peak channel in Figs. 3(a) and 3(b), assuming the nuclear reactions occur in the h-<sup>10</sup>BN and t-<sup>10</sup>BN domains, respectively. Indeed, we observed a linear relationship between the energy and the observed peak channel number. There are a few weak peaks (appear as shoulders) at the lower channel side of the individual peaks other than those marked. These are most likely due to an incomplete charge collection of the Li ions and  $\alpha$  particles generated by neutrons absorbed close to the surface of the detector, as pointed out in a simulation study.<sup>38</sup> But these weak peaks do not have a one-to-one relationship with the energies of the nuclear reaction products described in Eq. (1).

If our assumption of the nuclear reactions occurring in both h-BN and t-BN phases is correct, the measured ratio of the two slopes shown in Figs. 3(a) and 3(b) then represent the ratio between the energy bandgaps of h-BN and t-BN:

$$\frac{E_g(\text{h-BN})}{E_g(\text{t-BN})} = \frac{19.7}{17.6} = 1.1. \quad (4)$$

There have been very limited studies on the bandgap of t-BN. Most recently, first-principles calculations based on density functional and many-body perturbation theory were employed to examine the bandgaps of h-BN in various stacking sequences as well as the bandgap of t-BN<sup>31</sup> and the results provided  $E_g(\text{h-BN}) = 6.1$  eV for a perfectly hexagonal AA' stacking and  $E_g(\text{t-BN}) = 5.5$  eV, while the calculated  $E_g(\text{h-BN})$  agrees perfectly with experimental measurement results<sup>3,30</sup> and also with an earlier calculation result.<sup>7</sup> This band structure calculation thus provides  $\frac{E_g(\text{h-BN})}{E_g(\text{t-BN})} = 6.1/5.5 = 1.1$ .

The agreement between the gap ratios,  $\frac{E_g(\text{h-BN})}{E_g(\text{t-BN})}$ , deduced from the pulsed height spectrum shown in Fig. 2 and from this recent theoretical study<sup>31</sup> is remarkable, which reaffirms the interpretation that our thick h-BN films contain t-BN phase and  $E_g(\text{t-BN}) \approx 6.1/1.1 \approx 5.5$  eV. The presence of t-<sup>10</sup>BN domain in the thick h-<sup>10</sup>BN film has also been confirmed by the observation of a side peak at a lower diffraction angle than the main h-BN peak in the XRD  $\theta$ - $2\theta$  scan.<sup>35</sup>

In summary, the effects of the presence of t-BN domains in h-BN on the h-BN thermal neutron detector performance have been investigated. Two sets of 6 peak channels each were clearly observed in the pulsed height spectrum and identified to be linked with the charge carrier generation by

daughter particles in h-BN and t-BN domains, from which an energy bandgap value of 5.5 eV has been deduced for t-BN, consistent with a recent calculation result. More importantly, the improved device performance over the prior state-of-the-art attained here demonstrates that the presence of t-BN domains has little impact on the overall detection efficiency. The results imply that the crystal order and hence the lateral transport properties in the  $c$ -plane of t-BN are sufficiently good for the construction of detectors which utilize the lateral transport properties. The results indicate that there is a lot of room for improvements in the charge collection efficiencies of h-BN detectors if we can produce h-BN thick layers possessing a pure hexagonal phase and reduced concentrations of undesired impurities and deep level defects, including oxygen, carbon, and boron vacancies ( $V_B$ )-hydrogen complexes ( $V_B\text{-H}/V_B\text{-2H}$ ).<sup>11,12,18–20,30</sup> Such a realization would eventually allow us to construct detector strips with much wider widths and hence large area detectors without sacrificing the charge collection efficiencies. Nevertheless, the presence of the t-BN phase is not a showstopper for the further advancement of h-BN detector technologies as demonstrated by the present study.

The research is supported by DOE ARPA-E (#DE-AR0001257 and DE-AR0001552). Jiang and Lin are grateful to the AT&T Foundation for the support of Ed Whitacre and Linda Whitacre endowed chairs. The data that support the findings of this study are available within this manuscript.

- 1) (<https://nobelprize.org/prizes/physics/2014/press-release/>).
- 2) Department of Energy, *Wide Bandgap Semiconductors for Power Electronics, Quadrennial Technology Review* (Department of Energy, 2015), (<https://energy.gov/sites/default/files/2016/02/t29/QTR2015-6N-Wide-Bandgap-Semiconductors-for-Power-Electronics.pdf>).
- 3) T. Sugino, K. Tanioka, S. Kawasaki, and J. Shirafuji, *Jpn. Appl. Phys.* **36**, L463 (1997).
- 4) J. Li, S. Majety, R. Dahal, W. P. Zhao, J. Y. Lin, and H. X. Jiang, *Appl. Phys. Lett.* **101**, 171112 (2012).
- 5) K. Watanabe, T. Taniguchi, and H. Kanda, *Nat. Mater.* **3**, 404 (2004).
- 6) K. Watanabe, T. Taniguchi, and H. Kanda, *Nat. Photonics* **3**, 591 (2009).
- 7) B. Arnaud, S. Lebegue, P. Rabiller, and M. Alouani, *Phys. Rev. Lett.* **96**, 026402 (2006).
- 8) X. K. Cao, B. Clubine, J. H. Edgar, J. Y. Lin, and H. X. Jiang, *Appl. Phys. Lett.* **103**, 191106 (2013).
- 9) S. Majety, J. Li, X. K. Cao, R. Dahal, B. N. Pantha, J. Y. Lin, and H. X. Jiang, *Appl. Phys. Lett.* **100**, 061121 (2012).
- 10) H. X. Jiang and J. Y. Lin, *Semicond. Sci. Technol.* **29**, 084003 (2014).
- 11) A. Maity, S. J. Grenadier, J. Li, J. Y. Lin, and H. X. Jiang, *Prog. Quantum Electron.* **76**, 100302 (2021).
- 12) S. J. Grenadier, A. Maity, J. Li, J. Y. Lin, and H. X. Jiang, "Electrical transport properties of hexagonal boron nitride epilayers," *Ultrawide Bandgap Semiconductors*, ed. Y. Zhao, (Elsevier, Amsterdam, 2021), Vol. 107, Chap. 12.
- 13) T. T. Tran, C. Elbadawi, D. Totonjian, C. J. Lobo, G. Grosso, H. Moon, D. R. Englund, M. J. Ford, I. Aharonovich, and M. Toth, *ACS Nano* **10**, 7331 (2016).
- 14) N. R. Jungwirth, B. Calderon, Y. Ji, M. G. Spencer, M. E. Flatté, and G. D. Fuchs, *Nano Lett.* **16**, 6052 (2016).
- 15) Z. Shotan, H. Jayakumar, C. R. Conside, M. Mackoite, H. Fedder, J. Wrachtrup, A. Alkauskas, M. W. Doherty, V. M. Menon, and C. A. Meriles, *ACS Photonics* **3**, 2490 (2016).
- 16) Y. Wang, J. Lee, J. Berezovsky, and P. X.-L. Feng, *Appl. Phys. Lett.* **118**, 244003 (2021).
- 17) M. Kianinia et al., *ACS Photonics* **4**, 768 (2017).
- 18) A. Maity, T. C. Doan, J. Li, J. Y. Lin, and H. X. Jiang, *Appl. Phys. Lett.* **109**, 72101 (2016).

- 19) A. Tingsuwatit, A. Maity, S. J. Grenadier, J. Li, J. Y. Lin, and H. X. Jiang, *Appl. Phys. Lett.* **120**, 232103 (2022).
- 20) A. Maity, S. J. Grenadier, J. Li, J. Y. Lin, and H. X. Jiang, *Appl. Phys. Lett.* **116**, 142102 (2020).
- 21) G. F. Knoll, *Radiation Detection and Measurement* (Wiley, New York, 2010) 4th ed.
- 22) D. S. McGregor, R. T. Klann, H. K. Gersch, and Y. H. Yang, *Nucl. Instrum. Methods Phys. Res. A* **466**, 126 (2001).
- 23) P. Lunca-Popa, J. I. Brand, S. Balaz, L. G. Rosa, N. M. Boag, M. Bai, B. W. Robertson, and P. A. Dowben, *J. Phys. D: Appl. Phys.* **38**, 1248 (2005).
- 24) K. Osberg, N. Schemm, S. Balkir, J. O. Brand, M. S. Hallbeck, P. A. Dowben, and M. W. Hoffman, *IEEE Sensor J.* **6**, 1531 (2006).
- 25) R. Dahal, K. C. Huang, J. Clinton, N. LiCausi, J.-Q. Lu, Y. Danon, and I. Bhat, *Appl. Phys. Lett.* **100**, 243507 (2012).
- 26) R. J. Nikolic, A. M. Conway, C. E. Reinhardt, R. T. Graff, T. F. Wang, N. Deo, and C. L. Cheung, *Appl. Phys. Lett.* **93**, 133502 (2008).
- 27) A. M. Conway, T. F. Wang, N. Deo, C. L. Cheung, and R. J. Nikolic, *IEEE Trans. Nucl. Sci.* **56**, 2802 (2009).
- 28) D. S. McGregor, S. L. Bellinger, R. G. Fronk, L. Henson, D. Huddleston, T. Ochs, J. K. Shultis, T. J. Sobering, and R. D. Taylor, *Radiat. Phys. Chem.* **116**, 32 (2015).
- 29) J. Li, A. Maity, S. J. Grenadier, J. Y. Lin, and H. X. Jiang, *Appl. Phys. Lett.* **118**, 092102 (2021).
- 30) S. J. Grenadier, A. Maity, J. Li, J. Y. Lin, and H. X. Jiang, *Appl. Phys. Express* **15**, 051005 (2022).
- 31) K. A. Mengle and E. Kioupakis, *APL Mater.* **7**, 021106 (2019).
- 32) Y. Chen, H. Liang, X. Xia, H. Zhang, J. Shi, Q. Abbas, and G. Du, *J. Mater. Sci.* **28**, 14341 (2017).
- 33) N. Izyumskaya, D. Demchenko, S. Das, Ü. Özgür, V. Avrutin, and H. Morkoç, *Adv. Electron. Mater.* **3**, 1600485 (2017).
- 34) X. Yang, S. Nitta, K. Nagamatsu, S. Y. Bae, H. J. Lee, Y. Liu, M. Pristovsek, Y. Honda, and H. Amano, *J. Cryst. Growth* **482**, 1 (2018).
- 35) M. A. McKay, J. Li, J. Y. Lin, and H. X. Jiang, *J. Appl. Phys.* **127**, 0531032 (2020).
- 36) J. Clinton, "Optimization and characterization of a novel self powered solid state neutron detector," Ph.D. Dissertation Rensselaer Polytechnic Institute (2011).
- 37) T. C. Doan, S. Majety, S. Grenadier, J. Li, J. Y. Lin, and H. X. Jiang, *Nucl. Inst. Methods Phys. Res. A* **783**, 121 (2015).
- 38) G. Bhattarai, Ph.D. Dissertation in Physics and Chemistry The University of Missouri-Kansas City (2021), Chap. 3.